Aerosol optical tweezers constrain the evolution of liquid-liquid phase-separated morphologies in atmospheric particles

Kyle Gorkowski, 1,† Neil M. Donahue, 1 Ryan C. Sullivan 1,*

¹Center for Atmospheric Particle Studies, Carnegie Mellon University, Pittsburgh, PA, USA [†]Now at Atmospheric and Oceanic Sciences Department, McGill University, Montreal, QC, Canada

*Lead Contact & Corresponding Author: Ryan C. Sullivan; rsullivan@cmu.edu

Summary

5

10

15

20

Chemical models of atmospheric particles are vital in understanding the role of aerosol particles in atmospheric chemistry, air pollution, human health, and climate change. Advancing these models requires new frameworks that can realistically predict how critical particle properties evolve. We present such a framework for predicting particle phase separation and which morphology will prevail; this controls how each particle interacts with and affects the atmosphere. Aerosol optical tweezers experiments are used to probe the morphology within individual levitated particles. We studied the mixing behavior of α-pinene secondary organic aerosol (SOA) with different organic phases as relative humidity was varied to determine the interplay between polarity, miscibility, interfacial tension, and the resulting morphology. Using our measurments and literature data a general trend in morphology with increasing atmospheric oxidation was observed, from biphasic partially-engulfed – where both phases are immediately accessible to the gas phase – to biphasic core–shell, where the organic shell conceals the core, and finally to a single-phase homogeneous morphology.

KEYWORDS: atmospheric chemistry; environmental chemistry; particulate matter; air quality; climate change; organic aerosol; cavity-enhanced Raman spectroscopy; single-particle analysis; whispering gallery modes; morphology-dependent resonances; liquid-liquid phase separation

Introduction

25

30

35

40

45

Particles in the atmosphere reflect and absorb sunlight, activate to cloud droplets, nucleate ice crystals, and catalyze chemical reactions inaccessible in the gas phase.¹⁻³ Aerosols are thus major players in driving atmospheric chemistry, air pollution, and climate change.⁴⁻⁷ All of these important processes are governed by the composition at the gasparticle interface8, which changes as particle composition and morphology evolve. Morphology evolves with changes in water content and aerosol composition⁹⁻¹¹ that alter polarity, miscibility¹², and interfacial tensions¹³ during the roughly weeks-long¹⁴ atmospheric residence time of fine particles. The important interplay between these critical particle properties is not currently included in chemical transport models, which we rely on to understand the magnitude of all these important particle-driven processes and impacts. 15 Comprehensive experimental studies on individual particles that lead to new predictive frameworks are required before models can be advanced to represent the realistic evolution of particle morphology and its influence on aerosol-chemistry-cloudclimate interactions.

Atmospheric organic aerosols (OA) originate from direct emissions of primary organic aerosol (POA) and from the oxidation of organic vapors. The oxidation of organic

vapors generates less-volatile secondary organic aerosol (SOA). ^{16,17} Thousands of individual organic compounds constitute SOA, which is a major fraction of organic aerosol and total particulate matter mass. ^{18–20} In the atmosphere, SOA is mixed with POA, elemental carbon, inorganic salts, metals, minerals, and water, and the water content varies dramatically with relative humidity (RH). These suspended components combine into the broad category of particulate matter, with important but still poorly constrained effects on atmospheric chemistry, air pollution, human health, biogeochemistry, and climate change. ^{4–7}

50

55

60

65

Liquid aerosol particles are prevalent at tropospheric conditions. Depending on the constituents and thermodynamic conditions, a particle may undergo liquid-liquid phase separation (LLPS) into distinct chemical phases.^{21–27} We categorize these liquid particles as either single-phase homogeneous morphologies or liquid-liquid phase separated morphologies. 25,28-31 For a biphasic (phase-separated) particle, the two predominant equilibrium states are a core-shell or a partially-engulfed arrangement of the phases.³² Both phases are in direct contact with the gas phase in the latter morphology, while the core phase is completely concealed by the shell in a core-shell morphology. We have observed a core-shell morphology with α-pinene SOA as a shell on a squalane, aqueous NaCl, and aqueous glycerol droplets at 75% RH.9 In mixed inorganic-organic systems, phase separation results from poor miscibility, which is determined by the polarity and activity coefficients of the components and the water activity of the aqueous inorganic salt phase.¹² The water activity varies due to relative humidity changes, which can cause the organics to be salted out through LLPS at low RH.

When modeling small 10-50 nm particles acting as cloud condensation nuclei that produce cloud droplets, Ovadnevaite et al.³³ showed that biphasic morphology must be accounted for to close a gap between thermodynamic models and measurements. Biphasic morphologies also have strikingly different reactivity and reactive uptake kinetics compared to homogeneous particles when the organic phase forms a shell around the aqueous (water-rich) phase that drives hydrolysis reactions with important trace gases.⁸ The organic shell can play a significant role in impeding the reactive gas-particle uptake of hydrolyzable gases such as N₂O₅ and IEPOX – an epoxydiol produced from the oxidation of the dominant biogenic VOC, isoprene.^{10,11} The shell may also impede the exchange of semi-volatile organics and water between the particle and the surrounding atmosphere. These effects highlight the need to understand and predict the morphology of complex organic aerosol mixtures in the atmosphere.

Of particular interest in this study is how humidity and thus water content affects aerosol viscosity and morphology. Under atmospheric conditions, high viscosity (~10⁸ Pa s) aerosol have been observed.^{34–42} For a core–shell morphology, diffusion through the shell can dictate the equilibrium timescale of gas–particle partitioning between the core and the gas phase. In a glassy and hygroscopic particle, the water content plays a major plasticizing role that reduces viscosity and facilitates the transition to a liquid particle.^{43–45} This could result in drastically different equilibrium partitioning timescales during atmospheric humidity changes and cycling. Aerosol particle mixing experiments have shown an increase in the degree of mixing between two aerosol populations when the humidity changed from

20% to 40% RH.^{40,46} Therefore, it is vital that viscosity related experiments span the ambient humidity range.

Absorbed water can also increase the number of non-ideal intermolecular interactions within liquid mixtures, increasing the magnitude of the activity coefficients. For an organic carbon-only particle, this could lead to a homogeneous particle transitioning to a biphasic particle solely due to increasing humidity. Increasing RH causes the hygroscopic components to take up water and become more polar, potentially leading to phase separation from the less polar components. 9,27,47,48 In a mixed inorganic-organic particle the phase separation occurs as the RH decreases, concentrating the hygroscopic inorganic solute, and causing the more hydrophobic organic components to form a separate organic-rich phase. 12,23,49,50 For a biphasic particle, the organic phase hygroscopicity is vital as the water content will affect the resulting interfacial tension. The interfacial tension is analogous to surface tension except it describes the surface energy of the liquid–liquid interface. This interfacial tension is the determining factor, along with surface tensions, in forcing either a core–shell or partially-engulfed morphology upon LLPS. 29,30,32,51,52

Here we use the aerosol optical tweezers (AOT) to study the phase-separation humidity dependence of individual levitated droplets containing α -pinene SOA. The AOT can directly distinguish between the two primary biphasic morphologies and follow any changes as particle composition is varied by adding material through vapor condensation or particle coagulation, or through changing water content by adjusting the surrounding RH. This morphology analysis capability comes from the cavity-enhanced Raman spectrum

induced from the tweezed droplet that acts as an optical resonating cavity, thus providing a direct real-time morphology measurement of levitated droplets. 32,53,54 Alternate techniques to study phase-separation have used droplets placed on optical microscopy slides^{27,29,55–57} and more recently droplets suspended in oil within microfluidic devices.⁵⁸ Electron microscopy studies⁵⁹⁻⁶¹ suggest that the micron-scale equilibrium morphologies observed in our tweezers can be extrapolated down to 50 nm diameter particles (d_p) and thus are relevant for ambient atmospheric aerosol. Molecular dynamic simulations of nanoscale particles (d_p = 4-9 nm) also predict core-shell or partially-engulfed morphologies along with energetically higher variants (e.g. multiple organic islands).⁶² Our previous work⁹ on the morphology of tweezed droplets containing SOA focused on moderately high RH (~75%); here we extend these investigations to dryer conditions near 10% RH. We explore how the morphology of biphasic systems containing secondary organic aerosol (SOA) changes as water content decreases. We then combine our experimental observations with recent literature studies to predict the likely conditions for phase separation and the resulting morphologies of ambient mixed organic aerosol as it chemically evolves during atmospheric transport. This predictive framework can be readily incorporated into chemical transport models as it relies on commonly calculated parameters such as the oxygen-to-carbon atomic ratio (O:C) that represents organic carbon oxidation state⁶³, enabling more realistic representations of the effects of particulate matter on atmospheric chemistry and climate change.

Results

110

115

120

125

SOA Added to a Hydrophobic Organic Droplet

135

140

145

150

In our previous work⁹, we investigated α -pinene SOA added to a tweezed squalane droplet at intermediate RH. We deposited SOA to the squalane principally via coagulation of ~200 nm particles that nucleated in the AOT chamber and not via vapor condensation, as discussed in the Supplementary Information (SI). During this α -pinene SOA coagulation, the whispering gallery modes (WGMs) (also called morphology-dependent resonances) persisted in the Raman spectra retrieved from the droplet in real-time (acquired every 2 seconds). WGMs require spherical symmetry, and so their persistence indicates that the α pinene SOA particles had a low enough viscosity to promptly spread as they deposited on the tweezed droplet. There was also no evidence for the retardation of water diffusing from/to the aqueous core through the SOA shell, further indicating that the SOA did not create viscous transport limitations. That previous experiment was at 80% RH and thus included the plasticizing effect of water, reducing any viscous limitations and therefore promoting the spreading of the coagulating α -pinene SOA particles ($d_p \approx 200$ nm). Here we aim to maximize any possible viscous limitations in the α -pinene SOA system by conducting experiments at low RH.

Figure 1 displays the Raman spectra time series with the positions of the WGMs (indicated by the white dots), which are found by the peak searching algorithm. In Figure 1 the α -pinene SOA is formed at 12% RH, which should maximize the viscosity of the coagulating particles. The WGMs persist during the coagulation of the α -pinene SOA particles with the squalane droplet. This means the droplet remains relatively radially

symmetric and suggests that the coagulating α -pinene SOA particles spread rapidly (<2 s, the Raman spectrum acquisition time) into a homogeneous SOA shell.

155

160

165

Because the C-H hydrocarbon Raman band is narrow, we could not reliably identify enough WGMs (6 or more) for a successful core-shell fit. In the SI we show the Mie fit for a homogeneous optical model, which yields a sharp increase in fit error after the SOA addition begins. This increase in fit error (model failure, $\log_{10}(\chi^2_{red.}) > 0$) is characteristic of the formation of a core-shell morphology where the added SOA forms the shell, which renders the homogeneous model invalid. For the typical homogeneous droplet, $\log_{10}(\chi^2_{\rm red.})$ \leq -4. We show a similar experiment in the SI that confirms this core-shell morphology with valid core-shell Mie theory fitting of the observed WGMs (shell thickness of 147 ± 21 nm and $n_{650 nm}$ of 1.472 \pm 0.003). The opposite arrangement of an α -pinene SOA core and squalane shell does not fit the observed WGM behavior (see SI for details). The only difference between the two experiments is that the RH during the coagulation period for the experiment in the SI was 75%, and then the system was dried to 12% RH. The SOA collection experiment shown in Figure 1 was performed entirely at 12% RH. α-Pinene SOA forming the shell is consistent with our prior experiments at 80% RH.9

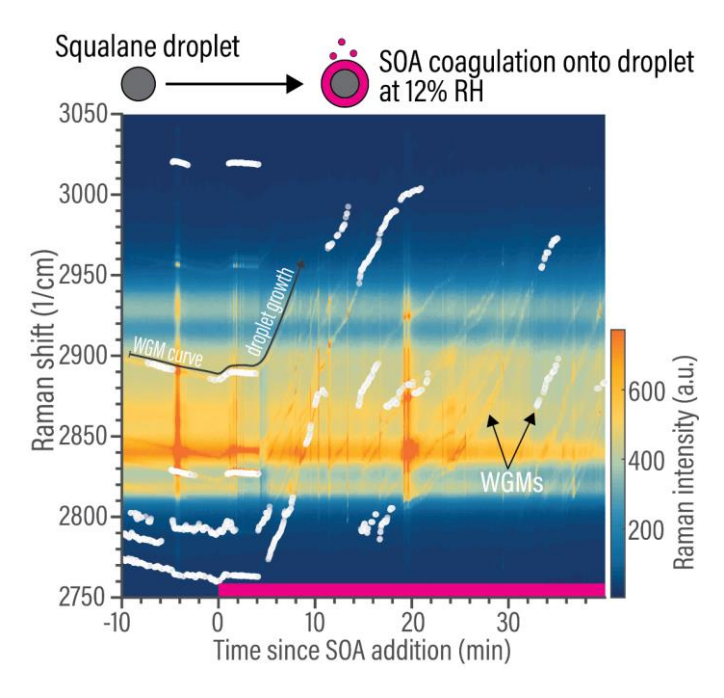


Figure 1. Raman spectral time series for a tweezed squalane droplet before and during α-pinene SOA *in situ* generation, at 12.5% RH. See the SI for the full time-series. The C–H hydrocarbon Raman mode center is at 2900 cm⁻¹, and the color scale indicates the intensity of the Raman signal versus Raman shift position. The bright white points indicate the positions of detectable whispering gallery modes (WGMs), although more can be found by visible inspection, as traced out by the gray line labeled as the WGM curve. The SOA flow reaction started at 0 min, indicated by the pink bar. The WGMs remain during the coagulation of SOA to the droplet, indicating a symmetrical morphology persists.

We next use the core–shell morphology (α -pinene SOA shell coating a squalane core) to interpret data during the SOA coagulation interval. The persistence of the WGMs means the droplet retained a spherical symmetry during the SOA particle coagulation. If the α -pinene SOA particles had not spread then they would have disrupted the WGM propagation; this disruption was shown for a different case in Gorkowski et al.⁹ and interpreted as WGM quenching caused by SOA coagulating and forming a stable emulsion of SOA particles inside an aqueous NaCl core, surrounded by an SOA shell. The formation of the emulsion in our previous work⁹ also confirms that particles are indeed coagulating onto the droplet. Condensational growth of the droplet is also occurring, but upper bound

170

calculations (in the SI) showed condensation cannot account for the majority of the SOA shell material. Therefore, the SOA particles (mode d_p = 200 nm) spread rapidly to form a single spherically symmetric surface shell, indicative of a more liquid behavior. This liquid behavior at low RH for α-pinene SOA is in contrast to some previous conclusions in the literature that the SOA is glassy (~10⁸ Pa s) when dry (<10% RH).^{34,42,64-67} This difference could be due to the high SOA mass concentrations (~10⁵ µg/m³) produced during our *in* situ SOA production and collection. Our high mass loadings would shift the range of SOA products in the particle phase to include higher volatility components, which would result in a lower viscosity.³⁶ More volatile SOA products are typically smaller and less oxidized, reducing the strength of the intermolecular interactions and thus plasticizing the particle.⁶⁸ However, aerosol mixing experiments at relatively low mass concentrations (20 - 80 μ g m⁻³) also showed no sign of diffusion limitations for α -pinene SOA at 20% RH⁴⁶, consistent with the liquid behavior observed here. These results do highlight the complexity of understanding the viscosity of SOA systems as it is influenced by the organic aerosol mass loading, hygroscopicity and water content, as well as how the viscosity is inferred from the measurement.

Miscibility of SOA in a Polar Organic Droplet

180

185

190

195

In our previous work⁹, we found that α -pinene SOA and aqueous glycerol phase-separated into a core–shell morphology at 73% RH. The water uptake by the glycerol phase increases its effective polarity, leading to more non-ideal interactions with the α -pinene SOA constituents, which explains why we previously observed a phase separation for that system.⁹ Here we seek to explore whether the glycerol plus α -pinene SOA system can

become miscible at low RH due to the removal of most of the water and the resulting reduction in polarity and water activity.

200

To probe the miscibility of the glycerol plus α -pinene SOA system we performed coagulation experiments at 12% RH, shown in Figure 2. We trapped a pure glycerol–water droplet at 80% RH and then ramped the RH down to 12% to dehydrate it. As the droplet

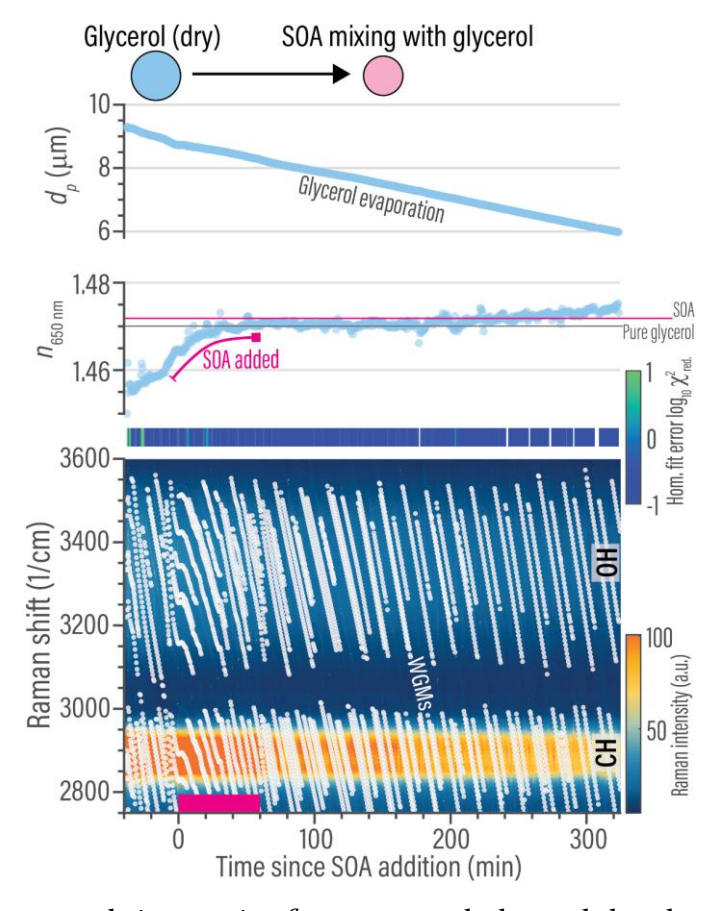


Figure 2. Raman spectral time series for a tweezed glycerol droplet with the addition of α -pinene SOA. The RH slowly decays from 14% RH at -40 min to 12% RH at 60 min. Raman spectra are shown in the bottom panel, and the white points indicate the positions of detectable whispering gallery modes (WGMs). The decreasing slope of the WGM traces indicates the droplet is evaporating. The α -pinene SOA flow reaction started at 0 min and lasted for 60 min, indicated by the pink bar. The droplet's refractive index and diameter retrieved from the WGM analysis are shown in the middle and top panels respectively. The fit error for the homogeneous model is shown in the green/blue bar, where consistently blue indicates a valid fit and green indicates an invalid fit to the model.

environment passed below 30% RH, the viscosity of the glycerol droplet increased (1 mPa s to 200 mPa s)⁶⁹, slowing evaporation of the remaining 12% by mass of water (inferred from the effective refractive index⁶⁹). This slow evaporation is why the effective refractive index ($n_{650 nm}$, of the homogeneous WGM fit) continued to increase ($n_{650 nm}$ = 1.33 for water) towards the refractive index of pure glycerol ($n_{650 nm}$ = 1.4701)⁷⁰, prior to α -pinene SOA addition at t = 0 min. Continued evaporation of water after SOA addition caused the refractive index to increase further. Also, we previously found that the refractive index of α -pinene SOA generated in our AOT at 80% RH is slightly higher than that of glycerol, $n_{650 nm}$ = 1.4718 ± 0.005. This also caused the droplet's refractive index to increase during the SOA addition period (0 to 60 min) in Figure 2.

The droplet continued to shrink long after SOA addition ceased, ultimately losing more than half of its volume. There was not enough water left for this to have been water loss and so it was likely glycerol evaporation. The increase in the refractive index after 200 minutes is consistent with the evaporation of glycerol, which would cause the mass fraction of SOA to increase and therefore increase the refractive index of the mixture. From our previous study⁹ the generated α -pinene SOA has a lower effective vapor pressure than glycerol (5.2 × 10⁻⁶ Pa vs. 133 Pa).

The absence of clear WGM peak splitting⁷¹ in the Raman spectra as the droplet size evolves indicates that the droplet remained homogeneous and that a core–shell morphology did not form. Peak splitting is readily observed by the WGMs splitting into two sets of wavelength positions that do not move in parallel as the droplet size evolves. The constant low fit error of the WGMs to a homogeneous Mie model quantitatively

supports this conclusion.⁷¹ An alternative explanation is that a core and shell formed with nearly the same refractive index; this is unlikely because the homogeneous fitting is highly sensitive to the refractive index (± 0.00067 in refractive index vs. an expected refractive index difference of 0.0017). A shift of 1.0 cm⁻¹ in the location of the WGMs – which we can resolve – corresponds to a change in *n* of 9.5×10^{-5} . To confirm that a single homogeneous phase should be present, we used the Aerosol Inorganic-Organic Mixtures Functional groups Activity Coefficients (AIOMFAC) model nested inside a phase equilibrium calculation (shown in the SI), which minimizes the Gibbs energy of the system. 49,57,72-74 We simulated glycerol mixing with a set of α -pinene SOA reaction products used to represent laboratory α-pinene SOA.^{12,75} This detailed thermodynamic calculation confirmed that glycerol and α -pinene SOA can form a single homogeneous phase in the absence of water (depending on the mixing ratios, details are provided in the SI). The reduction in water activity promotes the miscibility of the SOA and glycerol organic components, which phase separate under high RH and thus high water content conditions. A second calculation using Hansen solubility parameters and Flory-Huggins theory also confirmed a single-phase equilibrium (shown in the SI).⁷⁶ This experiment shows that for hygroscopic organic compounds, calculations of phase separation and morphology need to include the nonideal interactions of water along with the non-ideal interactions of different organic species, and how these change with varying water content.

Discussion

230

235

240

245

Atmospheric Oxidation and the Evolution of Interfacial Tension

Looking holistically at the experiments performed here and in Gorkowski et al.⁹, α -pinene SOA and nonpolar squalane form biphasic core–shell droplets at most humidities. Furthermore, α -pinene SOA and glycerol form core–shell droplets at 80% RH but homogeneous droplets at 12% RH. Humidity affects the miscibility but not the morphology of the separated phases; they remain spherically symmetrical as core–shell droplets. This phase separation and miscibility behavior is a result of SOA being a complex mixture with a range of molecular polarities.^{77,78} Even if some SOA components are miscible in the dominant chemical phase there can still be SOA components that are not, which leads to phase separation.

We can use the squalane results to explore the morphology of other systems similar to α -pinene SOA using the spreading coefficient framework. Spreading coefficients relate the morphology of the biphasic droplet to the surface tensions between each interface (a brief framework summary is provided in the SI, and discussed further in Gorkowski et al.³² and Reid et al.⁷⁹). For atmospheric systems containing two liquid phases, α and β , the equations simplify to a single inequality. We first define the difference between the surface tensions (i.e., liquid–air interface): $\Delta \sigma = \sigma_{\alpha} - \sigma_{\beta}$. Then for a partially-engulfed morphology, the interfacial tension between the two liquid phases must be greater than the difference in their surface tensions ($\sigma_{\alpha|\beta} > \Delta \sigma$) and for a core–shell morphology the opposite must hold ($\sigma_{\alpha|\beta} < \Delta \sigma$).

Spreading coefficients have been used to predict the biphasic morphologies of simple systems (aqueous inorganic salts and organics).^{30,79,80} For simple systems involving pure individual components (e.g., alcohols, ketones, carboxylic acids, esters, amines, or

aromatics)⁷⁹ the spreading coefficients and experiments indicate that a partially-engulfed morphology or core–shell is possible depending on the organic functionality. Our observations⁹ for α -pinene SOA mixture show that a core–shell morphology dominates. Previous studies with organic mixtures (O:C > 0.4) and inorganic salts showed a preponderance of core–shell morphologies after phase separation.^{25,27,29,55,56,61,81–84} In a complex organic mixture it is energetically favorable for the components that minimize the interfacial energies to partition to the liquid–liquid interface; this will keep $\sigma_{\alpha|\beta}$ small and therefore lead to a core–shell morphology. The same process of surface partitioning can act on the air–liquid interface, reducing surface tension of each phase. Both of these effects lower the surface energies of the interfaces, which favors the core–shell morphology. This process of partitioning to the liquid–liquid or air–liquid interface cannot occur when there is a single organic component.

For the experimentally observed morphology of a squalane core within an α -pinene SOA shell, the sum $\sigma_{SOA} + \sigma_{sq|SOA}$ must be less than the surface tension of squalane (σ_{sq} =28 mN/m 85). We can use this result to then predict the morphology of other systems, but first we need to fix $\sigma_{sq|SOA}$. A conservative approach is to use $\sigma_{sq|SOA}\approx0$, which will maximize the parameter space for partially-engulfed morphologies and mean $\sigma_{SOA}\approx28$ mN/m. From those assumptions, we can map out probable morphologies of other biphasic systems where the β liquid phase (water-poor) is similar to our SOA phase (see Fig. 3). For example, when the α phase is water, with a surface tension of 72 mN/m, then the interfacial tension has to be less than 44 mN/m for it to adopt a core–shell morphology. Note, this example is

a simplification as all liquid phases will have a mixture of components (inorganic+organic+water), which will result in surface tensions and an interfacial tension that are RH dependent. From our previous SOA additions to aqueous glycerol and aqueous NaCl droplets we observed a core–shell morphology and therefore conclude that the interfacial tension of α -pinene SOA and the water-rich phase is < 44 mN/m. This is the first constraint on the interfacial tension of a major type of SOA to our knowledge, and provides

290

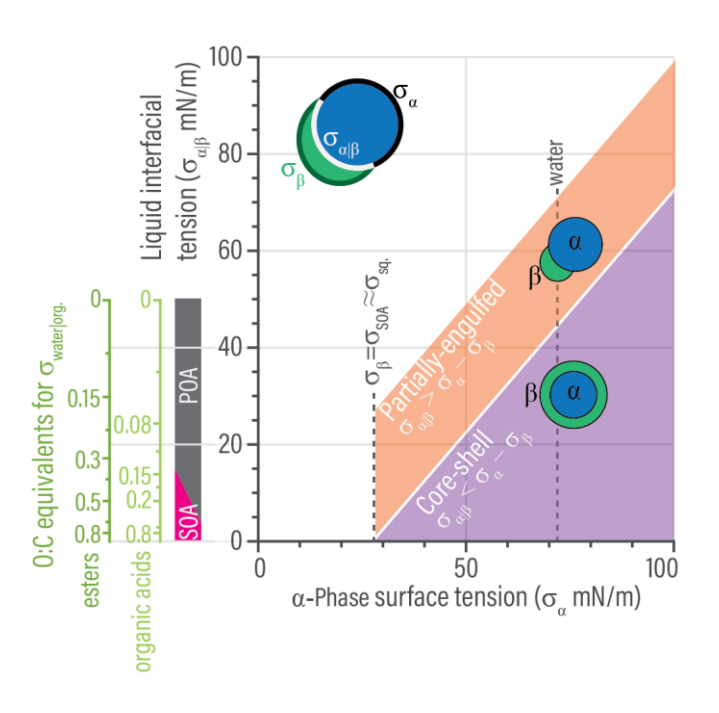


Figure 3. Possible morphologies for a biphasic particle composed of an α-phase (blue) of varying air–liquid surface tension (x-axis) and a β-phase (green) with an air–liquid surface tension of 28 mN/m (for $\sigma_{SOA} \approx \sigma_{sq}$) corresponding to an SOA like aerosol phase. The α-phase is assumed to always be the core, meaning that its surface tension is greater than that of the β-phase. In addition, the interfacial tension is assumed to always be less than the surface tension of the α-phase (i.e., $\sigma_{\alpha} > \sigma_{\beta} = \sigma_{SOA} \approx \sigma_{sq}$ and $\sigma_{\alpha} > \sigma_{\alpha|\beta}$). The green axis shows the equivalent oxygen-to-carbon ratio (O:C) trends for the interfacial tension between water and an organic compound (derived from exponential fits shown in the SI). We show organic acid trends (in $\sigma_{\alpha|\beta}$) as they are common in ambient OA systems. They are contrasted with organic esters, which were the organic group that had the highest interfacial tension for a given O:C in the compiled dataset. ^{86,87} For larger values of O:C a homogeneous morphology is expected ($\sigma_{\alpha|\beta} < 0$ is unphysical; as no liquid–liquid phase separation exists here).

a key parameter required to build a predictive model of SOA morphology and phase separations.

We compiled literature data^{86,87} for the interfacial tension between pure organic compounds and water and used it to relate interfacial tensions to the oxygen-to-carbon atomic ratio (O:C), a readily measured indicator of the degree of organic carbon oxidation state.^{63,86,87} Organic carbon is transformed from a less to a more highly oxidized state through atmospheric chemistry largely driven by free radicals such as the hydroxyl radical, as well as ozone and other reactive oxidants. This chemistry functionalizes the carbon backbone through the addition of polar functional groups, and fragmentation of carbon-carbon bonds through free radical oxidation is also possible. For organic molecules, O:C correlates with increasing intermolecular attraction through dipole–dipole interactions and hydrogen bonding. The molecular size and intermolecular interactions then determine bulk properties and behavior such as miscibility, phase separation,^{24,28,55} surface tension, viscosity,^{36,88} and molecular diffusivity.

We created an equivalent O:C axis in Figure 3 based on an exponential fit to the literature data, shown in the SI. This secondary O:C axis bounds possible morphologies that could be expected in ambient atmospheric organic aerosol. We used ester functional groups because they represent the largest range in interfacial tensions found in the literature datasets, though esters are not known to be common functionalities in organic aerosol. Instead alcohols, carbonyls, carboxylic acids, and peroxides are major functional groups produced by oxidation in atmospheric organic aerosol. The parameterized fits for

the interfacial tensions of alcohols, carboxylic acids, and ketones are also provided in the SI.

In the literature, there is a previous direct measurement of the surface tension of α -pinene SOA performed using atomic force microscopy (AFM).⁸⁹ The authors measured a surface tension of 27.5 mN/m at 10% RH and 44.4 mN/m at 67% RH for α -pinene SOA.⁸⁹ Our observations are not consistent with such a strong RH dependence for the surface tension of SOA because the morphology determined using the AOT did not change with an RH of 12% vs. 73%. This difference in surface tensions between the two experiments may be due to our different precursor concentrations and reaction conditions, and possible influences of the substrate the SOA was measured on using AFM. The AFM method used a smog chamber (batch reactor) with an ozone-to- α -pinene ratio of 1:1, generating ~10³ μ g/m³ of SOA. In contrast, in the AOT we used a flow reactor with an ozone limited reaction of 1:100 ozone to α -pinene ratio and generated ~10⁵ μ g/m³ of SOA. From our previous measurements⁹ the volatility of our *in situ* SOA is higher than typical smog chamber experiments. What remains unclear is how strongly volatility and surface tension are related.⁹⁰

Evolution of Particle Morphologies in the Atmosphere

320

325

330

335

Primary organic aerosol (POA) emitted to the atmosphere typically has a low O:C and is mostly composed of low-polarity hydrocarbons. Atmospheric chemical aging through heterogeneous oxidation, condensation of oxidized organic vapors, and photochemistry^{91,92} substantially increases the oxidation state of OA and thus O:C. This process converts primary non-polar POA into oxidized more-polar SOA and produces

highly oxidized SOA from gaseous semi-volatile organic compounds. ⁹³⁻⁹⁵ Mixing of POA and SOA with each other, and with aqueous inorganic phases, as well as other particle types (soot, dust, sea spray) also occurs substantially during atmospheric transport via coagulation. Submicron particles have atmospheric lifetimes of about a week, providing plenty of opportunities for aging and mixing to occur. Here we focus on the transition of low-polarity (hydrophobic) POA to high-polarity SOA, and their mixtures with soluble inorganic salts and water, representing a broad type of mixed aerosol ubiquitous throughout the lower atmosphere. Increases in the oxidation state can change miscibility and thus phase-separated states with aqueous inorganic phases, as well as alter interfacial tensions and thus the morphology of biphasic particles.

To gain a holistic understanding of how the O:C evolution effects the morphology we compiled literature observations $^{9,23,79,81-84,96,97,25,27,29,32,55,56,60,61}$ and calculations 79 of phase-separated morphologies. In this survey we included liquid–liquid phase separation of a water-rich α -phase (containing organics or inorganics) with a water-poor (organic-rich) β -phase. The full dataset is in the SI, and we present the summary in Table 1.

Table 1. Summary of predicted and observed particle morphologies for mixed organic–organic and organic–inorganic systems for different ranges of organic phase oxidation state.^a

Organic oxidation state	Partially- engulfed	Core-shell	Homogeneous	# systems
O:C < 0.4	56.6%	43.4%	0.0%	76
$0.4 \le O:C \le 0.8$	14.0%	57.9%	28.1%	57
0.8 < O:C	0.0%	0.0%	100.0%	5

^aSee SI for full literature dataset. 9,23,79,81-84,96,97,25,27,29,32,55,56,60,61

340

345

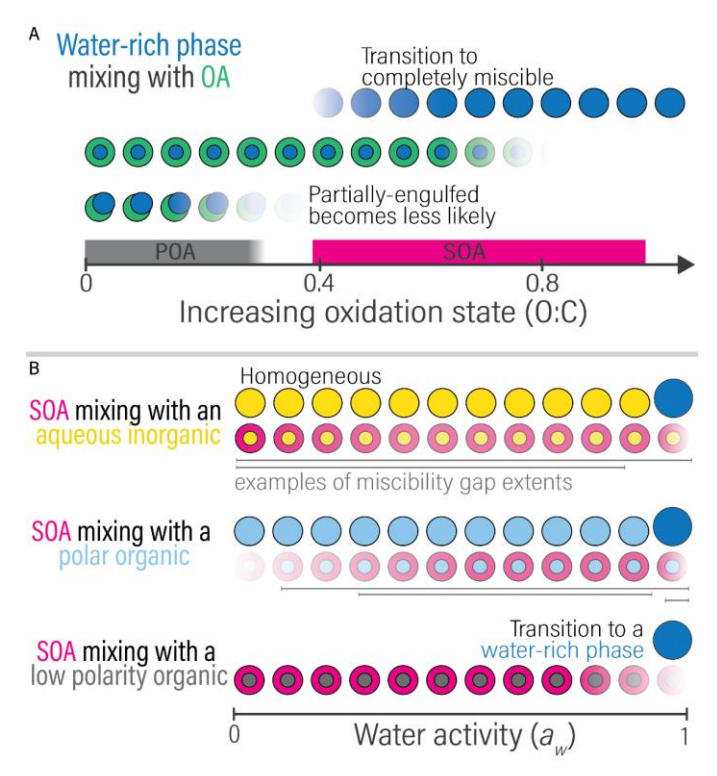


Figure 4. (A) Likely morphologies of an organic aerosol phase (green) mixing with a water-rich phase (blue). The morphologies as a function of O:C are based on the waterorganic interfacial tensions from Figure 3 and compiled observations tabulated in the SI. The water-rich phase can contain organics and inorganic salts. Core-shell and partially-engulfed morphologies are both possible at low O:C, but as O:C increases the core-shell morphology becomes predominant. As O:C continues to increase the phases become completely mixed. (B) The morphologies for an SOA phase (pink) mixing with a second phase as a function of water activity (a_w) . For SOA mixing with aqueous inorganic salts (yellow) the miscibility gaps tend to extend to zero water activity (a_w) and become miscible as a_w increases (examples ranges are shown by gray lines). If an SOA phase mixes with a polar organic phase (light blue), then the particle will likely be homogeneous at low a_w . However, there may be a miscibility gap as a_w increases, causing phase separation where the core-shell morphology is again predominant. When mixing with a low polarity organic phase (gray), the SOA phase forms the shell in a core-shell morphology. These mixtures will tend to form a water-rich homogeneous phase at water activities approaching one (corresponding to 100% RH), shown as a darker blue.

In Figure 4 we present a general schematic for the possible evolution of organic aerosol (OA) morphologies in the atmosphere based on the new experimental constraints on the interfacial tension of SOA and the spreading coefficient framework shown in Figure

3, and the literature results regarding LLPS and morphology summarized in Table 1. First, we explore a water-rich α -phase (containing inorganics or organics) mixing with different OA phases of increasing oxidation state. We depict the general O:C dependence of morphology in Figure 4A and examples of the RH dependence in Figure 4B.

For a relatively hydrophobic OA phase (O:C \ll 0.4), we predict phase-separated particles with either a partially-engulfed or a core–shell morphology (Figure 4A).⁷⁹ As O:C increases towards 0.4, the core–shell morphology becomes more prevalent because the interfacial tension decreases, as was shown in Figure 3. The sub-0.4 O:C region with relatively high interfacial tension will be dominated by primary organic aerosol (0.13 < O:C < 0.36 98). The partially-engulfed morphology can be observed in AOT experiments for droplets containing oleic acid (a proxy for POA from cooking) and an aqueous NaCl phase, for example.³² A partially-engulfed morphology requires a preponderance of highly surface active organic components and thus seems unlikely in the complex mixtures with a range of component O:C and functionality that represent realistic atmospheric aerosol particles, and rapidly undergo oxidative aging.

As O:C increases from 0.4 to 0.8, the biphasic systems of atmospheric interest transition to spherically symmetric morphologies.^{24,28,55} Note, partially-engulfed morphologies are possible in this O:C range as well, and it has been observed in a minority of cases (14%, see Table 1). The increasing polarity of the organic phase increases its miscibility with the water-rich phase. During this progression a completely homogeneous phase is possible, depending on the specific water activity and molecular composition. For ambient organic aerosol the average O:C value is 0.52 (range of 0.35 < O:C < 0.71) ⁹⁸, which

is within this transition region. Even higher in oxidation state is ambient SOA with an average O:C of 0.67.⁹⁸ Thus, the O:C of SOA corresponds to a low interfacial tension and therefore a spherically symmetrical morphology is predicted, either core–shell or a single homogeneous phase.^{23,84} Above an O:C of 0.8, the organics tend to be completely miscible in a water-rich phase (see Table 1), ensuring a homogeneous morphology.

In Figure 4B, we represent the general aspects for SOA gleaned from the AOT experiments and previous literature studies. We also use these diagrams to highlight some examples of the water activity dependence of phase separation, which is a hidden third axis in Figure 4A. The extent of the miscibility gap that leads to phase separation is not predicted in Figure 4B as that can more accurately be predicted with sophisticated thermodynamic equilibrium models, and confirmed using further AOT experiments. At infinite dilution with water, the organic phase will become miscible and result in a homogeneous morphology. That sets the limit as the water activity approaches one.

For our squalane experiments, we had a very low polarity organic (O:C = 0) plus oxidized α -pinene SOA, resulting in a core–shell morphology for both 12% and 80% RH. In this case, the droplet contains enough organic components of significantly different oxidation states and miscibilities, which leads to organic–organic phase separation. The second system we examined is a polar organic (glycerol) mixing with α -pinene SOA. At low RH the droplets are homogeneous, which is due to favorable Hansen solubility parameters (i.e. similar polarities and intermolecular interactions). As RH increases the glycerol phase takes up more water, increasing its polarity. The difference in polarity between the wet glycerol phase and α -pinene SOA results in more non-ideal molecular interactions,

culminating in a miscibility gap. The exact phase-separation RH depends on the relative mole fraction of the glycerol and the α -pinene SOA components. Thermodynamic modeling predicts that the two phases become miscible again as the droplet approaches a water activity of one. For biphasic inorganic–organic particles, the organics may be salted out and would only become a homogeneous phase as the RH increases.

405

410

415

420

Putting this succinctly, based on the current results and literature data we expect phase-separated particles to start as a partially-engulfed or core-shell morphology near primary emission sources, where POA dominates and O:C is low (O:C \ll 0.4). After atmospheric processing, particles tend to adopt a core-shell morphology when O:C exceeds 0.4. Further increases in O:C above 0.4 via atmospheric oxidative processing do not cause a core-shell particle to transition to a partially-engulfed particle; partially-engulfed morphologies do not form through oxidation. However, if O:C increases enough (>0.8) then the OA shell will dissolve into the water-rich phase, forming a homogenous singlephase morphology.²⁸ The additional influence of water content and thus water activity (i.e. RH) will also play a major role in this picture of morphology behavior. As the RH increases, phase-separated particles can become completely mixed via dilution into a water-rich phase. However, in some cases initially homogeneous particles can experience a miscibility gap and phase separate; this occurs when water is preferentially taken up by the hygroscopic components and results in phase separation. 12,99

This work has summarized our study of *in situ* generated α -pinene SOA that was directly collected onto a droplet trapped in the AOT for the first time, under low and high RH conditions. We consistently observe core–shell morphologies on aqueous and organic

systems with α -pinene SOA always as the shell. This provides the first constraints on the interfacial tension for complex SOA, which is the key parameter required to build a predictive framework for the atmospheric evolution of particle morphology. From a review of literature data, we reason that based on the oxidation state it is likely that the dominant morphology of OA on an aqueous particle in the atmosphere is core–shell with OA as the shell. For organic components, we highlight a need to understand how surface tension – and more importantly interfacial tension – is related to commonly measured ambient aerosol properties such as O:C, representing organic carbon oxidation state and polarity.

At a coarse resolution, with three O:C bins, the schematic outlined in Figure 4A can account for morphology in atmospheric aerosol models. To implement a high-resolution morphology model two main behaviors require clarification. The first is the role of organic mixtures in producing a partially-engulfed morphology. It is obvious from measurements that SOA mixtures prefer a core-shell morphology. What remains unknown is how diverse in molecular polarities the organic-rich phase needs to be before a core-shell morphology becomes more energetically favorable than a partially-engulfed morphology. The second is a simple representation of organic miscibility in water-rich phases, and how it depends on the O:C, molar mass, and molecular functionality. There has been a recent development of a reduced-complexity thermodynamic model by Gorkowski et al.⁷⁴, but it is not yet implemented in atmospheric chemical transport models. Our work provides a coarse modeling framework for aerosol morphology and highlights the two additional steps needed to realize a high-resolution aerosol morphology model. There are also additional

dependencies like particle size (below 50 nm) and acidity that affect morphology, but they are not well enough understood to even begin to add them to atmospheric aerosol models.

After the morphology and miscibility behaviors are parameterized, the subsequent impact on aerosol chemistry, air quality, and cloud condensation nuclei activity can be modeled. Particle morphology affects aerosol chemistry because an organic shell depresses the reactive gas-particle uptake of hydrolyzable gases such as N₂O₅ and IEPOX^{10,11}, and also influences condensation and partitioning through Raoult's Law.^{12,30,73,100–102} Accounting for this behavior may result in a lower predicted OA mass concentration, which affects how we understand aerosol sensitivity in climate studies. The organic shell morphology reduces the Kelvin effect (via the low organic surface tension), which promotes activation into a cloud droplet of the hygroscopic core phase.³³ This clearer understanding of molecular properties and the resulting morphologies will fully realize the influence of phase-separated aerosol particles in Earth's coupled atmosphere–climate system.

Experimental Procedures

450

455

460

465

We have previously described the novel design and characteristics of the Carnegie Mellon University (CMU) AOT system in Gorkowski et al.³² Our AOT system uses a 532 nm laser with a 100x (NA 1.25) oil immersion microscope objective. The objective forms an optical gradient force trap approximately 40 microns above the coverslip inside the AOT chamber. We use a Condensational Monodisperse Aerosol Generator (CMAG; TSI, Inc.) to generate glycerol and squalane droplets. We control the RH in the chamber by varying the

flow ratio of dry to humidified air. The RH is measured at the chamber inlet using a hydrometer (Vaisala).

To add SOA to a trapped droplet, we use the AOT chamber as a flow reactor. The α -pinene vapor, which is introduced into the top of the chamber, undergoes dark ozonolysis and produces SOA directly inside the AOT chamber. The gas and particle-phase products then condense onto or collide with the tweezed droplet, modifying its composition. During a typical ozonolysis experiment, the ozone concentration in the AOT is 55 ppm_v, and the α -pinene vapor concentration is 500 ppm_v, based on the saturated vapor pressure of α -pinene and volumetric flow rates. Two SOA characterization experiments, with no tweezed droplet, used a scanning mobility particle sizer (TSI, Inc.) to measure the α -pinene SOA size distribution inside the AOT chamber under the same SOA production conditions used in the other experiments. This SOA coagulation method was explained in detail in Gorkowski et al.⁹

We record the Raman scattered light induced by the 532 nm trapping laser – which includes the resonant whispering gallery modes (WGMs) – from the tweezed droplet at 0.5 Hz using a spectrograph (Princeton Acton spectrograph with PIXIS CCD detector) with a 1200 grooves/mm diffraction grating. The droplet acts as a high finesse optical cavity and amplifies the Raman scattering, which leads to standing waves near the droplet's surface that amplify discrete wavelengths in the Raman spectrum, i.e. WGMs. 103,104 Any radial inhomogeneities in the droplet dampen the WGMs. 9,105,106 The WGM amplification process is completely quenched in partially-engulfed morphologies because they are asymmetrical

droplets.^{30,32,51} Core-shell morphologies are radially symmetric, therefore retaining the WGMs.^{25,32,71}

490

495

500

505

Both the symmetrical core-shell and homogeneous morphologies produce WGMs, so we used our previously developed fitting algorithm to distinguish between the two. 71 The difference is often visually obvious when the WGM positions change with droplet diameter; the WGMs in homogeneous droplets evolve parallel to each other, whereas the WGMs in core-shell droplets do not.⁷¹ This is because different modes have different characteristic penetration depths and thus experience a different average index of refraction. Further, when fitting WGMs of a core-shell droplet to a homogeneous Mie model, the result is a consistently high fit error and unphysical parameters.^{25,32,71} There are also limitations in fitting the WGMs when only the hydrocarbon (C-H) Raman scattering mode is measured. The C-H Raman mode is narrower and more congested than the O-H Raman mode, which leads to fewer WGMs available to fit. To still gain insight into the pure organic systems we use a priori information on the refractive indices of the initial pure core phase (e.g., glycerol, squalane) to reduce the parameter space. This method is applied to our squalane experiments performed here. For homogeneous droplets, size is typically determined with an uncertainty of 0.05% in diameter, and 0.06% for refractive index.⁷¹ For core-shell morphologies, the accuracy of the retrieved shell parameters is reduced, with typical uncertainty levels of 0.24% in shell diameter, 3.8% in core diameter, and 0.37% in the refractive indices.⁷¹

Acknowledgements. Kyle Gorkowski was supported in part by a Bertucci Fellowship from Carnegie Mellon University's College of Engineering. This research was supported by the National Science Foundation (Awards CHE-1213718 & CHE-1554941). The AIOMFAC equilibrium model used here was developed by Andreas Zuend and we are thankful for his support in modeling the experimental systems.

Author Contributions. KG and RCS conceived the project and experiments; KG performed the experiments and data analysis; KG, NMD, and RCS interpreted the results and constructed the modeling framework. KG drafted the manuscript, and all authors provided input to the writing.

Declaration of Interests. The authors declare no competing interests.

Supporting Information. Includes an expanded discussion for the coagulation experiments of α -pinene SOA onto a squalane droplet and includes the full experimental timeseries. We also present the spreading coefficient framework, the compiled interfacial tension data, and the thermodynamic modeling outputs. The compiled literature review of biphasic morphologies is tabulated as well.

References

510

515

520

- 1. Rastak, N., Pajunoja, A., Acosta Navarro, J.C., Ma, J., Song, M., Partridge, D.G., Kirkevåg, A., Leong, Y., Hu, W.W., Taylor, N.F., *et al.* (2017). Microphysical explanation of the RH-dependent water affinity of biogenic organic aerosol and its importance for climate. Geophys. Res. Lett. 44, 5167–5177. https://doi.org/10.1002/2017GL073056.
- 2. Shrivastava, M., Cappa, C.D., Fan, J., Goldstein, A.H., Guenther, A.B., Jimenez, J.L., Kuang, C., Laskin, A., Martin, S.T., Ng, N.L., *et al.* (2017). Recent advances in understanding secondary organic aerosol: Implications for global climate forcing. Rev. Geophys. *55*, 509–559. https://doi.org/10.1002/2016RG000540.
 - 3. Mülmenstädt, J., Sourdeval, O., Delanoë, J., and Quaas, J. (2015). Frequency of occurrence of rain from liquid-, mixed-, and ice-phase clouds derived from A-Train satellite retrievals. Geophys. Res. Lett. 42, 6502–6509. https://doi.org/10.1002/2015GL064604.
 - 4. Kolb, C.E., and Worsnop, D.R. (2012). Chemistry and Composition of Atmospheric Aerosol Particles. Annu. Rev. Phys. Chem. *63*, 471–491.

- https://doi.org/10.1146/annurev-physchem-032511-143706.
- 5. Pöschl, U. (2005). Atmospheric Aerosols: Composition, Transformation, Climate and Health Effects. Angew. Chemie Int. Ed. 44, 7520–7540. https://doi.org/10.1002/anie.200501122.
- Myhre, G., Shindell, D., Bréon, F.-M., Collins, W., Fuglestvedt, J., Huang, J., Koch, D., Lamarque, J.-F., Lee, D., Mendoza, B., et al. (2013). Anthropogenic and Natural Radiative Forcing. In Climate Change 2013 The Physical Science Basis, Intergovernmental Panel on Climate Change, ed. (Cambridge: Cambridge University Press), pp. 659–740. https://doi.org/10.1017/CBO9781107415324.018.
- 7. Pope, C.A., Ezzati, M., and Dockery, D.W. (2009). Fine-Particulate Air Pollution and Life Expectancy in the United States. N. Engl. J. Med. *360*, 376–386. https://doi.org/10.1056/NEJMsa0805646.
 - 8. Whalley, L., Stone, D., and Heard, D. (2012). New Insights into the Tropospheric Oxidation of Isoprene: Combining Field Measurements, Laboratory Studies, Chemical Modelling and Quantum Theory. In Topics in current chemistry, V. F. McNeill and P. A. Ariya, eds. (Berlin, Heidelberg: Springer Berlin Heidelberg), pp. 55–95. https://doi.org/10.1007/128_2012_359.
 - 9. Gorkowski, K., Donahue, N.M., and Sullivan, R.C. (2017). Emulsified and Liquid–Liquid Phase-Separated States of α-Pinene Secondary Organic Aerosol Determined Using Aerosol Optical Tweezers. Environ. Sci. Technol. *51*, 12154–12163. https://doi.org/10.1021/acs.est.7b03250.
- 560 10. Gaston, C.J., and Thornton, J.A. (2016). Reacto-Diffusive Length of N 2 O 5 in Aqueous Sulfate- and Chloride-Containing Aerosol Particles. J. Phys. Chem. A *120*, 1039–1045. https://doi.org/10.1021/acs.jpca.5b11914.

- 11. Park, S.-C., Burden, D.K., and Nathanson, G.M. (2007). The Inhibition of N2O5 Hydrolysis in Sulfuric Acid by 1-Butanol and 1-Hexanol Surfactant Coatings. J. Phys. Chem. A *111*, 2921–2929. https://doi.org/10.1021/jp068228h.
 - 12. Zuend, A., and Seinfeld, J.H. (2012). Modeling the gas-particle partitioning of secondary organic aerosol: the importance of liquid-liquid phase separation. Atmos. Chem. Phys. *12*, 3857–3882. https://doi.org/10.5194/acp-12-3857-2012.
- 13. Boyer, H., Wexler, A., and Dutcher, C.S. (2015). Parameter Interpretation and Reduction for a Unified Statistical Mechanical Surface Tension Model. J. Phys. Chem. Lett. *6*, 3384–3389. https://doi.org/10.1021/acs.jpclett.5b01346.
 - 14. Schum, S.K., Zhang, B., Džepina, K., Fialho, P., Mazzoleni, C., and Mazzoleni, L.R. (2018). Molecular and physical characteristics of aerosol at a remote free troposphere site: implications for atmospheric aging. Atmos. Chem. Phys. *18*, 14017–14036. https://doi.org/10.5194/acp-18-14017-2018.
 - 15. Tsigaridis, K., Daskalakis, N., Kanakidou, M., Adams, P.J., Artaxo, P., Bahadur, R.,

- Balkanski, Y., Bauer, S.E., Bellouin, N., Benedetti, A., *et al.* (2014). The AeroCom evaluation and intercomparison of organic aerosol in global models. Atmos. Chem. Phys. *14*, 10845–10895. https://doi.org/10.5194/acp-14-10845-2014.
- 580 16. Gentner, D.R., Isaacman, G., Worton, D.R., Chan, A.W.H., Dallmann, T.R., Davis, L., Liu, S., Day, D.A., Russell, L.M., Wilson, K.R., *et al.* (2012). Elucidating secondary organic aerosol from diesel and gasoline vehicles through detailed characterization of organic carbon emissions. Proc. Natl. Acad. Sci. *109*, 18318–18323. https://doi.org/10.1073/pnas.1212272109.
- Hallquist, M., Wenger, J.C., Baltensperger, U., Rudich, Y., Simpson, D., Claeys, M., Dommen, J., Donahue, N.M., George, C., Goldstein, A.H., *et al.* (2009). The formation, properties and impact of secondary organic aerosol: current and emerging issues. Atmos. Chem. Phys. *9*, 5155–5236. https://doi.org/10.5194/acp-9-5155-2009.
- 18. Zhang, Q., Jimenez, J.L., Canagaratna, M.R., Allan, J.D., Coe, H., Ulbrich, I., Alfarra, M.R., Takami, A., Middlebrook, A.M., Sun, Y.L., *et al.* (2007). Ubiquity and dominance of oxygenated species in organic aerosols in anthropogenically-influenced Northern Hemisphere midlatitudes. Geophys. Res. Lett. *34*, 1–6. https://doi.org/10.1029/2007GL029979.
- 19. Saathoff, H., Naumann, K.-H., Moehler, O., Jonsson, A.M., Hallquist, M., Kiendler-Scharr, A., Mentel, T.F., Tillmann, R., and Schurath, U. (2009). Temperature dependence of yields of secondary organic aerosols from the ozonolysis of alphapinene and limonene. Atmos. Chem. Phys. 9, 1551–1577. https://doi.org/10.5194/acp-9-1551-2009.
- 20. Surratt, J.D., Murphy, S.M., Kroll, J.H., Ng, N.L., Hildebrandt, L., Sorooshian, A., Szmigielski, R., Vermeylen, R., Maenhaut, W., Claeys, M., *et al.* (2006). Chemical Composition of Secondary Organic Aerosol Formed from the Photooxidation of Isoprene. J. Phys. Chem. A *110*, 9665–9690. https://doi.org/10.1021/jp061734m.
- 21. Hekayati, J., Roosta, A., and Javanmardi, J. (2016). Liquid–liquid equilibria in the quinary aqueous two-phase system of poly(ethylene glycol) 6000+sodium sulfate+water in the presence of glucose and ethanol: Experimental investigation and thermodynamic modeling. Thermochim. Acta 625, 47–52. https://doi.org/10.1016/j.tca.2015.12.013.
- 22. Bateman, A.P., Gong, Z., Liu, P., Sato, B., Cirino, G., Zhang, Y., Artaxo, P., Bertram, A.K., Manzi, A.O., Rizzo, L. V., *et al.* (2015). Sub-micrometre particulate matter is primarily in liquid form over Amazon rainforest. Nat. Geosci. *9*, 34–37. https://doi.org/10.1038/ngeo2599.
- 23. Song, M., Marcolli, C., Krieger, U.K., Zuend, A., and Peter, T. (2012). Liquid-liquid phase separation in aerosol particles: Dependence on O:C, organic functionalities, and compositional complexity. Geophys. Res. Lett. *39*, 1–5. https://doi.org/10.1029/2012GL052807.

- 24. You, Y., Smith, M.L., Song, M., Martin, S.T., and Bertram, A.K. (2014). Liquid–liquid phase separation in atmospherically relevant particles consisting of organic species and inorganic salts. Int. Rev. Phys. Chem. *33*, 43–77. https://doi.org/10.1080/0144235X.2014.890786.
- 520 25. Stewart, D.J., Cai, C., Nayler, J., Preston, T.C., Reid, J.P., Krieger, U.K., Marcolli, C., and Zhang, Y.-H.H.Y.-H.H. (2015). Liquid–Liquid Phase Separation in Mixed Organic/Inorganic Single Aqueous Aerosol Droplets. J. Phys. Chem. A 119, 4177–4190. https://doi.org/10.1021/acs.jpca.5b01658.
- 26. Schill, G.P., and Tolbert, M.A. (2013). Heterogeneous ice nucleation on phaseseparated organic-sulfate particles: effect of liquid vs. glassy coatings. Atmos. Chem. Phys. *13*, 4681–4695. https://doi.org/10.5194/acp-13-4681-2013.
 - 27. Renbaum-Wolff, L., Song, M., Marcolli, C., Zhang, Y., Liu, P.F., Grayson, J.W., Geiger, F.M., Martin, S.T., and Bertram, A.K. (2016). Observations and implications of liquid–liquid phase separation at high relative humidities in secondary organic material produced by α-pinene ozonolysis without inorganic salts. Atmos. Chem. Phys. *16*, 7969–7979. https://doi.org/10.5194/acp-16-7969-2016.

- 28. You, Y., and Bertram, A.K. (2015). Effects of molecular weight and temperature on liquid–liquid phase separation in particles containing organic species and inorganic salts. Atmos. Chem. Phys. *15*, 1351–1365. https://doi.org/10.5194/acp-15-1351-2015.
- 635 29. Song, M., Marcolli, C., Krieger, U.K., Lienhard, D.M., and Peter, T. (2013). Morphologies of mixed organic/inorganic/aqueous aerosol droplets. Faraday Discuss. *165*, 289–316. https://doi.org/10.1039/c3fd00049d.
- 30. Kwamena, N.-O.A., Buajarern, J., and Reid, J.P. (2010). Equilibrium morphology of mixed organic/inorganic/aqueous aerosol droplets: investigating the effect of relative humidity and surfactants. J. Phys. Chem. A 114, 5787–5795. https://doi.org/10.1021/jp1003648.
 - 31. Metcalf, A.R., Boyer, H.C., and Dutcher, C.S. (2016). Interfacial Tensions of Aged Organic Aerosol Particle Mimics Using a Biphasic Microfluidic Platform. Environ. Sci. Technol. *50*, 1251–1259. https://doi.org/10.1021/acs.est.5b04880.
- 645 32. Gorkowski, K., Beydoun, H., Aboff, M., Walker, J.S., Reid, J.P., and Sullivan, R.C. (2016). Advanced aerosol optical tweezers chamber design to facilitate phase-separation and equilibration timescale experiments on complex droplets. Aerosol Sci. Technol. 50, 1327–1341. https://doi.org/10.1080/02786826.2016.1224317.
- Ovadnevaite, J., Zuend, A., Laaksonen, A., Sanchez, K.J., Roberts, G., Ceburnis, D., Decesari, S., Rinaldi, M., Hodas, N., Facchini, M.C., *et al.* (2017). Surface tension prevails over solute effect in organic-influenced cloud droplet activation. Nature *546*, 637–641. https://doi.org/10.1038/nature22806.
 - 34. Reid, J.P., Bertram, A.K., Topping, D.O., Laskin, A., Martin, S.T., Petters, M.D., Pope,

- F.D., and Rovelli, G. (2018). The viscosity of atmospherically relevant organic particles. Nat. Commun. *956*, 1–14. https://doi.org/10.1038/s41467-018-03027-z.
 - 35. Power, R.M., Simpson, S.H., Reid, J.P., and Hudson, a. J. (2013). The transition from liquid to solid-like behaviour in ultrahigh viscosity aerosol particles. Chem. Sci. 4, 2597–2604. https://doi.org/10.1039/c3sc50682g.
- 36. Davies, J.F., Miles, R.E.H., Haddrell, A.E., and Reid, J.P. (2013). Influence of organic films on the evaporation and condensation of water in aerosol. Proc. Natl. Acad. Sci. U. S. A. *110*, 8807–8812. https://doi.org/10.1073/pnas.1305277110.

- 37. Virtanen, A., Joutsensaari, J., Koop, T., Kannosto, J., Yli-Pirilä, P., Leskinen, J., Mäkelä, J.M., Holopainen, J.K., Pöschl, U., Kulmala, M., *et al.* (2010). An amorphous solid state of biogenic secondary organic aerosol particles. Nature *467*, 824–827. https://doi.org/10.1038/nature09455.
- 38. Shiraiwa, M., Li, Y., Tsimpidi, A.P., Karydis, V.A., Berkemeier, T., Pandis, S.N., Lelieveld, J., Koop, T., and Pöschl, U. (2017). Global distribution of particle phase state in atmospheric secondary organic aerosols. Nat. Commun. 8, 1–7. https://doi.org/10.1038/ncomms15002.
- 670 39. Liu, P., Li, Y.J., Wang, Y., Gilles, M.K., Zaveri, R.A., Bertram, A.K., and Martin, S.T. (2016). Lability of secondary organic particulate matter. Proc. Natl. Acad. Sci. *113*, 12643–12648. https://doi.org/10.1073/pnas.1603138113.
- 40. Ye, Q., Robinson, E.S., Ding, X., Ye, P., Sullivan, R.C., and Donahue, N.M. (2016). Mixing of secondary organic aerosols versus relative humidity. Proc. Natl. Acad. Sci. 113, 12649–12654. https://doi.org/10.1073/pnas.1604536113.
 - 41. Grayson, J.W., Zhang, Y., Mutzel, A., Renbaum-Wolff, L., Böge, O., Kamal, S., Herrmann, H., Martin, S.T., and Bertram, A.K. (2016). Effect of varying experimental conditions on the viscosity of alpha-pinene derived secondary organic material. Atmos. Chem. Phys. *16*, 6027–6040. https://doi.org/10.5194/acp-16-6027-2016.
- 42. Zhang, Y., Sanchez, M.S., Douet, C., Wang, Y., Bateman, A.P., Gong, Z., Kuwata, M., Renbaum-Wolff, L., Sato, B.B., Liu, P.F., *et al.* (2015). Changing shapes and implied viscosities of suspended submicron particles. Atmos. Chem. Phys. *15*, 7819–7829. https://doi.org/10.5194/acp-15-7819-2015.
- 43. Moridnejad, A., Preston, T.C., and Krieger, U.K. (2017). Tracking Water Sorption in Glassy Aerosol Particles using Morphology-Dependent Resonances. J. Phys. Chem. A *121*, 8176–8184. https://doi.org/10.1021/acs.jpca.7b06774.
 - 44. Lee, H.D., Ray, K.K., and Tivanski, A. V. (2017). Solid, Semisolid, and Liquid Phase States of Individual Submicrometer Particles Directly Probed Using Atomic Force Microscopy. Anal. Chem. 89, 12720–12726. https://doi.org/10.1021/acs.analchem.7b02755.
 - 45. Song, Y.C., Haddrell, A.E., Bzdek, B.R., Reid, J.P., Bannan, T., Topping, D.O., Percival,

- C., and Cai, C. (2016). Measurements and Predictions of Binary Component Aerosol Particle Viscosity. J. Phys. Chem. A *120*, 8123–8137. https://doi.org/10.1021/acs.jpca.6b07835.
- 695 46. Ye, Q., Upshur, M.A., Robinson, E.S., Geiger, F.M., Sullivan, R.C., Thomson, R.J., and Donahue, N.M. (2018). Following Particle-Particle Mixing in Atmospheric Secondary Organic Aerosols by Using Isotopically Labeled Terpenes. Chem 4, 318–333. https://doi.org/10.1016/j.chempr.2017.12.008.
- 47. Hodas, N., Zuend, a., Mui, W., Flagan, R.C., and Seinfeld, J.H. (2014). Influence of particle phase state on the hygroscopic behavior of mixed organic–inorganic aerosols. Atmos. Chem. Phys. *14*, 32935–32977. https://doi.org/10.5194/acpd-14-32935-2014.
- 48. Song, M., Ham, S., Andrews, R.J., You, Y., and Bertram, A.K. (2018). Liquid-liquid phase separation in organic particles containing one and two organic species: importance of the average O:C. Atmos. Chem. Phys. *18*, 12075–12084. https://doi.org/10.5194/acp-18-12075-2018.

- 49. Zuend, A., and Seinfeld, J.H. (2013). A practical method for the calculation of liquid-liquid equilibria in multicomponent organic-water-electrolyte systems using physicochemical constraints. Fluid Phase Equilib. *337*, 201–213. https://doi.org/10.1016/j.fluid.2012.09.034.
- 50. Hodas, N., Zuend, a., Mui, W., Flagan, R.C., and Seinfeld, J.H. (2015). Influence of particle-phase state on the hygroscopic behavior of mixed organic–inorganic aerosols. Atmos. Chem. Phys. *15*, 5027–5045. https://doi.org/10.5194/acp-15-5027-2015.
- Dennis-Smither, B.J., Hanford, K.L., Kwamena, N.A., Miles, R.E.H., and Reid, J.P. (2012). Phase, morphology, and hygroscopicity of mixed oleic acid/sodium chloride/water aerosol particles before and after ozonolysis. J. Phys. Chem. A *116*, 6159–6168. https://doi.org/10.1021/jp211429f.
- 52. Krieger, U.K., Marcolli, C., and Reid, J.P. (2012). Exploring the complexity of aerosol particle properties and processes using single particle techniques. Chem. Soc. Rev. 41, 6631–6662. https://doi.org/10.1039/c2cs35082c.
 - 53. Cai, C., Tan, S., Chen, H., Ma, J., Wang, Y., Reid, J.P., and Zhang, Y. (2015). Slow water transport in MgSO 4 aerosol droplets at gel-forming relative humidities. Phys. Chem. Phys. *17*, 29753–29763. https://doi.org/10.1039/C5CP05181A.
- 725 54. Meresman, H., Hudson, A.J., and Reid, J.P. (2011). Spectroscopic characterization of aqueous microdroplets containing inorganic salts. Analyst *136*, 3487–3495. https://doi.org/10.1039/c0an00843e.
 - 55. Bertram, A.K., Martin, S.T., Hanna, S.J., Smith, M.L., Bodsworth, A., Chen, Q., Kuwata, M., Liu, A., You, Y., and Zorn, S.R. (2011). Predicting the relative humidities

- of liquid-liquid phase separation, efflorescence, and deliquescence of mixed particles of ammonium sulfate, organic material, and water using the organic-to-sulfate mass ratio of the particle and the O:C of the organic. Atmos. Chem. Phys. *11*, 10995–11006. https://doi.org/10.5194/acp-11-10995-2011.
- 56. You, Y., Renbaum-Wolff, L., Carreras-Sospedra, M., Hanna, S.J., Hiranuma, N., Kamal, S., Smith, M.L., Zhang, X., Weber, R.J., Shilling, J.E., *et al.* (2012). Images reveal that atmospheric particles can undergo liquid-liquid phase separations. Proc. Natl. Acad. Sci. U. S. A. *109*, 13188–13193. https://doi.org/10.1073/pnas.1206414109.
- 57. Song, M., Marcolli, C., Krieger, U.K., Zuend, A., and Peter, T. (2012). Liquid-liquid phase separation and morphology of internally mixed dicarboxylic acids/ammonium sulfate/water particles. Atmos. Chem. Phys. *12*, 2691–2712. https://doi.org/10.5194/acp-12-2691-2012.
 - 58. Nandy, L., and Dutcher, C.S. (2018). Phase Behavior of Ammonium Sulfate with Organic Acid Solutions in Aqueous Aerosol Mimics Using Microfluidic Traps. J. Phys. Chem. B *122*, 3480–3490. https://doi.org/10.1021/acs.jpcb.7b10655.
- 745 59. Veghte, D.P., Altaf, M.B., and Freedman, M.A. (2013). Size Dependence of the Structure of Organic Aerosol. J. Am. Chem. Soc. *135*, 16046–16049. https://doi.org/10.1021/ja408903g.
- 60. Altaf, M.B., Zuend, A., and Freedman, M.A. (2016). Role of nucleation mechanism on the size dependent morphology of organic aerosol. Chem. Commun. *52*, 9220–9223. https://doi.org/10.1039/C6CC03826C.
 - 61. Altaf, M.B., and Freedman, M.A. (2017). Effect of Drying Rate on Aerosol Particle Morphology. J. Phys. Chem. Lett. 8, 3613–3618. https://doi.org/10.1021/acs.jpclett.7b01327.
- 62. Karadima, K.S., Mavrantzas, V.G., and Pandis, S.N. (2019). Insights into the morphology of multicomponent organic and inorganic aerosols from molecular dynamics simulations. Atmos. Chem. Phys. *19*, 5571–5587. https://doi.org/10.5194/acp-19-5571-2019.
- 63. Kroll, J.H., Donahue, N.M., Jimenez, J.L., Kessler, S.H., Canagaratna, M.R., Wilson, K.R., Altieri, K.E., Mazzoleni, L.R., Wozniak, A.S., Bluhm, H., *et al.* (2011). Carbon oxidation state as a metric for describing the chemistry of atmospheric organic aerosol. Nat. Chem. *3*, 133–139. https://doi.org/10.1038/nchem.948.
 - 64. Vaden, T.D., Imre, D., Beranek, J., Shrivastava, M., and Zelenyuk, A. (2011). Evaporation kinetics and phase of laboratory and ambient secondary organic aerosol. Proc. Natl. Acad. Sci. *108*, 2190–2195. https://doi.org/10.1073/pnas.1013391108.
- 765 65. Abbatt, J.P.D., Lee, A.K.Y., and Thornton, J.A. (2012). Quantifying trace gas uptake to tropospheric aerosol: recent advances and remaining challenges. Chem. Soc. Rev. 41, 6555–6581. https://doi.org/10.1039/c2cs35052a.

66. Abramson, E., Imre, D., Beránek, J., Wilson, J., and Zelenyuk, A. (2013). Experimental determination of chemical diffusion within secondary organic aerosol particles. Phys. Chem. Chem. Phys. *15*, 2983–2991. https://doi.org/10.1039/c2cp44013j.

770

785

- 67. Pajunoja, A., Malila, J., Hao, L., Joutsensaari, J., Lehtinen, K.E.J., and Virtanen, A. (2014). Estimating the Viscosity Range of SOA Particles Based on Their Coalescence Time. Aerosol Sci. Technol. 48, 1–4. https://doi.org/10.1080/02786826.2013.870325.
- 68. Koop, T., Bookhold, J., Shiraiwa, M., and Pöschl, U. (2011). Glass transition and phase state of organic compounds: dependency on molecular properties and implications for secondary organic aerosols in the atmosphere. Phys. Chem. Chem. Phys. *13*, 19238–55. https://doi.org/10.1039/clcp22617g.
 - 69. Haynes W. M. (2017). CRC Handbook of Chemistry and Physics, 97th Edition.
- 70. Rheims, J., Köser, J., and Wriedt, T. (1997). Refractive-index measurements in the near-IR using an Abbe refractometer. Meas. Sci. Technol. 8, 601–605. https://doi.org/10.1088/0957-0233/8/6/003.
 - 71. Gorkowski, K., Donahue, N.M., and Sullivan, R.C. (2018). Emerging investigator series: determination of biphasic core–shell droplet properties using aerosol optical tweezers. Environ. Sci. Process. Impacts 20, 1512–1523. https://doi.org/10.1039/C8EM00166A.
 - 72. Zuend, A., Marcolli, C., Booth, A.M., Lienhard, D.M., Soonsin, V., Krieger, U.K., Topping, D.O., McFiggans, G., Peter, T., and Seinfeld, J.H. (2011). New and extended parameterization of the thermodynamic model AIOMFAC: calculation of activity coefficients for organic-inorganic mixtures containing carboxyl, hydroxyl, carbonyl, ether, ester, alkenyl, alkyl, and aromatic functional groups. Atmos. Chem. Phys. *11*, 9155–9206. https://doi.org/10.5194/acp-11-9155-2011.
 - 73. Zuend, A., Marcolli, C., Luo, B.P., and Peter, T. (2008). A thermodynamic model of mixed organic-inorganic aerosols to predict activity coefficients. Atmos. Chem. Phys. 8, 4559–4593. https://doi.org/10.5194/acp-8-4559-2008.
- 795 74. Gorkowski, K., Preston, T.C., and Zuend, A. (2019). RH-dependent organic aerosol thermodynamics via an efficient reduced-complexity model. Atmos. Chem. Phys. Discuss., 1–37. https://doi.org/10.5194/acp-2019-495.
- 75. Rastak, N., Pajunoja, A., Acosta Navarro, J.C., Ma, J., Song, M., Partridge, D.G., Kirkevåg, A., Leong, Y., Hu, W.W., Taylor, N.F., *et al.* (2017). SI: Microphysical explanation of the RH-dependent water affinity of biogenic organic aerosol and its importance for climate. Geophys. Res. Lett. *44*, 5167–5177. https://doi.org/10.1002/2017GL073056.
- 76. Ye, J., Gordon, C.A., and Chan, A.W.H. (2016). Enhancement in Secondary Organic Aerosol Formation in the Presence of Preexisting Organic Particle. Environ. Sci. Technol. *50*, 3572–3579. https://doi.org/10.1021/acs.est.5b05512.

- 77. Suda, S.R., Petters, M.D., Matsunaga, A., Sullivan, R.C., Ziemann, P.J., and Kreidenweis, S.M. (2012). Hygroscopicity frequency distributions of secondary organic aerosols. J. Geophys. Res. Atmos. 117, 1–14. https://doi.org/10.1029/2011JD016823.
- 810 78. Suda, S.R., Petters, M.D., Yeh, G.K., Strollo, C., Matsunaga, A., Faulhaber, A., Ziemann, P.J., Prenni, A.J., Carrico, C.M., Sullivan, R.C., *et al.* (2014). Influence of Functional Groups on Organic Aerosol Cloud Condensation Nucleus Activity. Environ. Sci. Technol. *48*, 10182–10190. https://doi.org/10.1021/es502147y.
- 79. Reid, J.P., Dennis-Smither, B.J., Kwamena, N.-O.A., Miles, R.E.H., Hanford, K.L., and Homer, C.J. (2011). The morphology of aerosol particles consisting of hydrophobic and hydrophilic phases: hydrocarbons, alcohols and fatty acids as the hydrophobic component. Phys. Chem. Chem. Phys. *13*, 15559–15572. https://doi.org/10.1039/clcp21510h.
- 80. Buajarern, J., Mitchem, L., and Reid, J.P. (2007). Characterizing Multiphase Organic/Inorganic/Aqueous Aerosol Droplets. J. Phys. Chem. A *111*, 9054–9061. https://doi.org/10.1021/jp074366a.
 - 81. Ciobanu, V.G., Marcolli, C., Krieger, U.K., Weers, U., and Peter, T. (2009). Liquid–Liquid Phase Separation in Mixed Organic/Inorganic Aerosol Particles. J. Phys. Chem. A *113*, 10966–10978. https://doi.org/10.1021/jp905054d.
- 82. Pant, A., Fok, A., Parsons, M.T., Mak, J., and Bertram, A.K. (2004). Deliquescence and crystallization of ammonium sulfate-glutaric acid and sodium chloride-glutaric acid particles. Geophys. Res. Lett. *31*, 1–4. https://doi.org/10.1029/2004GL020025.
- 83. Fard, M.M., Krieger, U.K., and Peter, T. (2017). Kinetic Limitation to Inorganic Ion Diffusivity and to Coalescence of Inorganic Inclusions in Viscous Liquid–Liquid Phase-Separated Particles. J. Phys. Chem. A *121*, 9284–9296. https://doi.org/10.1021/acs.jpca.7b05242.

- 84. You, Y., Renbaum-Wolff, L., and Bertram, A.K. (2013). Liquid-liquid phase separation in particles containing organics mixed with ammonium sulfate, ammonium bisulfate, ammonium nitrate or sodium chloride. Atmos. Chem. Phys. *13*, 11723–11734. https://doi.org/10.5194/acp-13-11723-2013.
- 85. Korosi, G., and Kovats, E.S. (1981). Density and surface tension of 83 organic liquids. J. Chem. Eng. Data *26*, 323–332. https://doi.org/10.1021/je00025a032.
- 86. Girifalco, L. a., and Good, R.J. (1957). A Theory for the Estimation of Surface and Interfacial Energies. I. Derivation and Application to Interfacial Tension. J. Phys. Chem. *61*, 904–909. https://doi.org/10.1021/j150553a013.
 - 87. Shahid, M.Z., Usman, M.R., Akram, M.S., Khawaja, S.Y., and Afzal, W. (2017). Initial Interfacial Tension for Various Organic–Water Systems and Study of the Effect of Solute Concentration and Temperature. J. Chem. Eng. Data *62*, 1198–1203.

https://doi.org/10.1021/acs.jced.6b00703.

- 845 88. Rothfuss, N.E., and Petters, M.D. (2017). Influence of Functional Groups on the Viscosity of Organic Aerosol. Environ. Sci. Technol. *51*, 271–279. https://doi.org/10.1021/acs.est.6b04478.
- 89. Hritz, A.D., Raymond, T.M., and Dutcher, D.D. (2016). A method for the direct measurement of surface tension of collected atmospherically relevant aerosol particles using atomic force microscopy. Atmos. Chem. Phys. *16*, 9761–9769. https://doi.org/10.5194/acp-16-9761-2016.
 - 90. Kidd, C., Perraud, V., Wingen, L.M., and Finlayson-Pitts, B.J. (2014). Integrating phase and composition of secondary organic aerosol from the ozonolysis of -pinene. Proc. Natl. Acad. Sci. *III*, 7552–7557. https://doi.org/10.1073/pnas.1322558111.
- 91. McFiggans, G., Mentel, T.F., Wildt, J., Pullinen, I., Kang, S., Kleist, E., Schmitt, S., Springer, M., Tillmann, R., Wu, C., *et al.* (2019). Secondary organic aerosol reduced by mixture of atmospheric vapours. Nature *565*, 587–593. https://doi.org/10.1038/s41586-018-0871-y.
- 92. Praske, E., Otkjær, R. V., Crounse, J.D., Hethcox, J.C., Stoltz, B.M., Kjaergaard, H.G., and Wennberg, P.O. (2018). Atmospheric autoxidation is increasingly important in urban and suburban North America. Proc. Natl. Acad. Sci. *115*, 64–69. https://doi.org/10.1073/pnas.1715540115.
- 93. Jimenez, J.L., Canagaratna, M.R., Donahue, N.M., Prevot, a S.H., Zhang, Q., Kroll, J.H., DeCarlo, P.F., Allan, J.D., Coe, H., Ng, N.L., *et al.* (2009). Evolution of Organic Aerosols in the Atmosphere. Science *326*, 1525–1529. https://doi.org/10.1126/science.1180353.
 - 94. Bianchi, F., Kurtén, T., Riva, M., Mohr, C., Rissanen, M.P., Roldin, P., Berndt, T., Crounse, J.D., Wennberg, P.O., Mentel, T.F., *et al.* (2019). Highly Oxygenated Organic Molecules (HOM) from Gas-Phase Autoxidation Involving Peroxy Radicals: A Key Contributor to Atmospheric Aerosol. Chem. Rev. *119*, 3472–3509. https://doi.org/10.1021/acs.chemrev.8b00395.
 - 95. Donahue, N.M., Robinson, A.L., and Pandis, S.N. (2009). Atmospheric organic particulate matter: From smoke to secondary organic aerosol. Atmos. Environ. *43*, 94–106. https://doi.org/10.1016/j.atmosenv.2008.09.055.
- 875 96. Bodsworth, A., Zobrist, B., and Bertram, A.K. (2010). Inhibition of efflorescence in mixed organic–inorganic particles at temperatures less than 250 K. Phys. Chem. Chem. Phys. *12*, 12259–12266. https://doi.org/10.1039/c0cp00572j.
- 97. Parsons, M.T., Mak, J., Lipetz, S.R., and Bertram, A.K. (2004). Deliquescence of malonic, succinic, glutaric, and adipic acid particles. J. Geophys. Res. Atmos. *109*, 1–880 8. https://doi.org/10.1029/2003jd004075.
 - 98. Canagaratna, M.R., Jimenez, J.L., Kroll, J.H., Chen, Q., Kessler, S.H., Massoli, P.,

- Hildebrandt Ruiz, L., Fortner, E., Williams, L.R., Wilson, K.R., *et al.* (2015). Elemental ratio measurements of organic compounds using aerosol mass spectrometry: characterization, improved calibration, and implications. Atmos. Chem. Phys. *15*, 253–272. https://doi.org/10.5194/acp-15-253-2015.
- 99. Petters, M.D., Wex, H., Carrico, C.M., Hallbauer, E., Massling, A., McMeeking, G.R., Poulain, L., Wu, Z., Kreidenweis, S.M., and Stratmann, F. (2009). Towards closing the gap between hygroscopic growth and activation for secondary organic aerosol Part 2: Theoretical approaches. Atmos. Chem. Phys. *9*, 3999–4009. https://doi.org/10.5194/acp-9-3999-2009.

- 100. Yan, W., Topphoff, M., Rose, C., and Gmehling, J. (1999). Prediction of vapor-liquid equilibria in mixed-solvent electrolyte systems using the group contribution concept. Fluid Phase Equilib. *162*, 97–113. https://doi.org/10.1016/S0378-3812(99)00201-0.
- 895 101. Zuend, A., Marcolli, C., Peter, T., and Seinfeld, J.H. (2010). Computation of liquid-liquid equilibria and phase stabilities: Implications for RH-dependent gas/particle partitioning of organic-inorganic aerosols. Atmos. Chem. Phys. *10*, 7795–7820. https://doi.org/10.5194/acp-10-7795-2010.
- 102. Compernolle, S., Ceulemans, K., and Müller, J.F. (2009). Influence of non-ideality on condensation to aerosol. Atmos. Chem. Phys. 9, 1325–1337. https://doi.org/10.5194/acp-9-1325-2009.
 - 103. Wills, J.B., Knox, K.J., and Reid, J.P. (2009). Optical control and characterisation of aerosol. Chem. Phys. Lett. *481*, 153–165. https://doi.org/10.1016/j.cplett.2009.09.020.
 - 104. Yang, J.J., Huang, M., Yu, J., and Lan, Y.Z. (2011). Surface whispering-gallery mode. Europhys. Lett. *96*, 1–5. https://doi.org/10.1209/0295-5075/96/57003.
 - 105. Mishchenko, M.I., Liu, L., and Mackowski, D.W. (2014). Morphology-dependent resonances of spherical droplets with numerous microscopic inclusions. Opt. Lett. 39, 1701–1704. https://doi.org/10.1364/OL.39.001701.
- 106. Ngo, D., and Pinnick, R.G. (1994). Suppression of scattering resonances in inhomogeneous microdroplets. J. Opt. Soc. Am. A 11, 1352–1359. https://doi.org/10.1364/JOSAA.11.001352.